Structure, texture and strength of Mg-5.8Zn-0.65Zr alloy after hot-to-warm multi-step isothermal forging and isothermal rolling to large strains

M. Markushev[a,*], D. Nugmanov[a], O. Sitdikov[a], A. Vinogradov[b]

[a] *Institute for Metals Superplasticity Problems, Russian Academy of Sciences, Ufa, 450001, Russia*

[b] *Department of Mechanical and Industrial Engineering, Norwegian University of Science and Technology - NTNU, 7491 Trondheim, Norway*

Aiming at improving deformability of wrought Mg alloys, the commercial hot-pressed alloy MA14 (ZK60) was subjected to hot/warm severe plastic deformation (SPD) to a total true strain of 9. The processing schedule involved a combination of two-stage multi-step isothermal forging performed at 400 and 300 °C and subsequent isothermal rolling at 300 °C. The evolution of the microstructure, texture and mechanical properties were investigated. SPD resulted in a highly homogeneous microstructure with the size of equiaxed grain (subgrain) reduced down ~2.5 μm (1.5 μm). The strong initial fiber texture was transformed into the weak pyramidal texture during forging operation and then to the typical basal texture during further rolling. Changes in the distribution of excess phases are also reported. In response to microstructural changes induced by SPD, the ductility of the alloy enhanced substantially without compromising the strength. Unlike conventional semi-products having a high anisotropy of mechanical properties, the proposed processing method resulted in the isotropic yield stress and elongation to failure. The nature of grain refinement and the structure-property relations emphasizing the effects of the grain structure and texture on the tensile strength and its anisotropy are discussed.

1. Introduction

Magnesium alloys are among the most perspective structural light-weight materials nowadays. A combination of low density, high specific strength and excellent damping capacity makes them highly attractive for wider applications in aerospace and automotive manufacturing, consumer electronics and medical materials engineering [1]. However, despite the impressive potential, the uptake of wrought Mg alloys by industry has been rather sluggish. One of the main reasons for that is the poor deformability of magnesium cast and wrought products due to a limited number of slip systems in the hexagonal close-packed (hcp) crystal lattice, pronounced asymmetry of the mechanical response caused by a polar nature of mechanical twinning, and strong unfavorable deformation texture developed in the products during commercial processing [1,2].

An effective strategy, which has gained a great popularity in the recent two decades, aiming at enhancing strength and ductility of metals and alloys is based on significant grain refinement. Ultrafine-grain and even nanocrystalline (UFG and NC) structures having grain (subgrain) size less than 1 and 0.1 μm, respectively, have been produced in different materials, including magnesium based alloys, via so-called severe plastic deformation (SPD) imparting large effective strains $e > 1$ onto a working peace [3–6]. Among many other SPD techniques, multi-step isothermal forging (MIF) has been proven quite efficient to produce industrially scalable amount of UFG and NC bulk billets. For sheet productions, a highly potent approach utilizes a combination of MIF and isothermal rolling (IR), which has been sucessfully applied for manufacturing of hcp zirconium and titanium based alloys [6].

Effect of SPD on the microstructure and properties of magnesium alloys has been just scarcely studied to date. In view of increasing efficiency of practical applications of SPD techniques, it is challenging to explore the capacity of industrially scalable methods such as MIF and IR for magnesium alloys manufacturing. The present work is aimed at investigating the evolution of the microstructure, texture and tensile mechanical properties of a commercial Mg-Zn-Zr alloy after SPD. This alloy is considered as a representative of a class of wrought Mg alloys. The SPD processing used in the present work included thermo-mechanical treatment combining two isothermal processes – MIF and IR – performed at warm-to-hot conditions at temperatures above the solvus temperature of the main strengthening β ($MgZn_2$)-phase.

2. Experimental procedure

Billets of 90 mm diameter and 170 mm long were cut from a commercial hot-pressed rod of MA14[1] (Mg-5.8Zn-0.65Zr (%, wt.)) alloy. They were then MIF processed to the equivalent strains of 4.2 and 3.0 in two sequential steps at 400 and 300 °C, respectively, using a hydraulic press with an isothermal die set. Each step included several deformation cycles of preheated in the air furnace billets, involving successive settings with deformation axes changing after each cycle (see [7,8] for more detail). The plates of $15 \times 20 \times 25$ mm^3 dimensions were machined from the MIF-processed billets and then rolled to e ~1.6 in the direction perpendicular to the last setting with a speed of 2 mm/s at 300 °C. Isothermal conditions under rolling were provided by heaters built-in in the clamping rollers. The specimens and working rollers were pre-heat in a furnace to desired temperature.

The alloy microstructure and texture were analyzed in the longitudinal and transverse sections of the initial pressed, forged and rolled billets using the scanning electron microscope (SEM) Tescan Mira LM equipped with the electron backscattered diffraction (EBSD) system and the HKL CHANNEL 5 software. The grain and subgrain size, volume fraction of recrystallized grains and grain boundary misorientation distributions were obtained from EBSD data. Low- and high-angle boundaries (LABs and HABs) were identified as boundaries having a misorientation angle, Θ, from 2 to 15° and greater than 15°, respectively. The subgrain and grain size was evaluated from EBSD data by converting area measurements into a "circle equivalent diameter" (with the mean of the equivalent diameters of each of the individual grains) as recommended by ISO 13067:2011 [9] and implemented in the orientation image microscopy software by Oxford Instruments [10]. The orientation maps were constructed by the analysis of 6–7 Kikuchi lines in the EBSD patterns using the database for pure Mg. The points corresponding to the second phases were not taken into account in grain (sub-grain) size measurements. The fraction of twin boundaries was determined for both primary {10$\bar{1}$2} (~86° ± 2°), (~66.5° ± 2°) and secondary {10$\bar{1}$1} (~30° ± 2°), (~37° ± 2°) twins [11,12]. The pole figures were obtained using combined data of five to six 100×100 μm^2 EBSD maps generated from different areas of the initial and SPD processed material to ensure representative grain statistics for the texture analysis [13]. The second phases were characterized by the equivalent diameter, d (with the mean value denoted by $\bar{d}$), the area fraction S, the partial area fraction s_i/S of particles (phases) with different sizes and), specific area fraction (s/S) of phases of different size, as well as by the the interparticle spacing $\lambda = d\sqrt{\pi/6S}$ assuming a spherical particle shape [14]. All these quantities were averaged for both excess and secondary (precipitates) phases, ranging from 20 nm to several micrometers. These variables were evaluated from backscattered electron (BSE) SEM images obtained in both longitudinal and transverse sections using the ImageJ analytical software using the standard stereological algorithms. The S value was determined as a ratio of the total area of the secondary phases identified by the BSE detector to the scanned area of the metallographic section. The data sample included the readings from not less than 6000 particles for each alloy's structural state and each section. The precipitates were also detected by transmission electron microscopy (TEM) (JEOL 2000EX). The specimens for SEM and TEM observations were prepared by conventional mechanical thinning and grinding ended by electro-polishing under 20 V applied voltage in a solution of nitric acid in methanol at 5 °C using a Tenupol-5 twin-jet polisher.

Tensile tests were carried out at ambient temperature on the Instron 5982 screw-driven testing machine using dog-bone shape specimens with $10 \times 2 \times 2$ mm^3 gage part. The specimens were cut from the SPD processed billets and sheets in either longitudinal or transverse
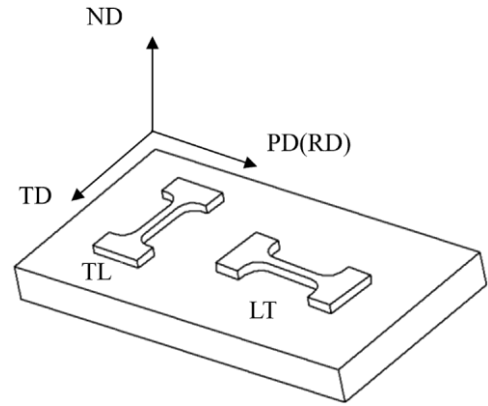
Fig. 1. Axes in the initial and processed billets and scheme of tensile samples cutting. PD (RD), TD and ND are the pressing (rolling), transverse and normal directions, respectively. LT and TL are the standard abbreviations of longitudinal and transverse tensile samples.

directions corresponding to the processing axes - LT and TL, respectively, Fig. 1.

3. Results and discussion

3.1. Microstructure

Typical optical microscopy images and colour coded EBSD orientation image maps representing the grain structure in the longitudinal section of the initial hot pressed rod and SPD-processed billets are shown in Fig. 2. The initial hot-pressed (HP) rod has a partially recrystallized structure with coarse elongated grains up to 1 mm long and 50 μm thick surrounded by fine equiaxed grains 6.5 ± 0.5 μm in size, Fig. 2a. The sub-grains with a mean diameter of 5.5 μm can be observed inside the elongated grains as well as in some coarse equiaxed grains. Although the recrystallized structure does not prevail over the area of observation, the grain boundary distribution reveals a large fraction of high-angle boundaries (V_{HAB} = 50%) with a relatively large average angle of boundary misorientations (Θ_{av} ~35°), Fig. 3a. After MIF, the microstructure became predominantly recrystallized and fine-grained, Fig. 2b. It contained of 80–85% equiaxed grains of 5 μm in Besides, forging changed the grain boundary spectrum so that Θ_{av} and

diameter and of 20% of unrecrystallized grains with 2–3 μm subgrains. V_{HAB} increased to 43° and 69%, respectively, Fig. 3b. Considering the microstructure evolution, whereby the transverse low-angle dislocation sub-boundaries are formed in the preferably oriented elongated grains and then subsequently transformed into HABs with the increase of strain, the main mechanism of the alloy grain refinement is identified as continuous dynamic recrystallization [7,8,15,16]. It is worthy noticing that the resultant grain boundary misorientations spectrum exhibited a clear peak at about 86°, Fig. 3, corresponding to tensile twin boundaries according to the Brandon criterion [17]. By no means can this serve as a proof of mechanical twinning occurring possibly during processing. The twins also cannot be unambiguously identified from optical microscopy images shown in Fig. 2 (even though some twin-like lamellae can be recognized on the micrographs) as well, since both crystallographic orientation and boundary plane inclination must be known. However, based on a large experimental database, the consensus seems to be that twinning play a significant role in the nucleation of dynamically recrystallized grains during warm and even hot deformation of Mg alloys [16,18–20]. Thus, it seems plausible to suppose that dynamic recrystallization originated from mechanical twinning influences the microstructure development during MIF. We should also notice that under conditions of dynamic recrystallization, new grains continuously replace the most work-hardened ones and, thus, deformation twins lose their original morphology. They therefore can be hardly observed in the
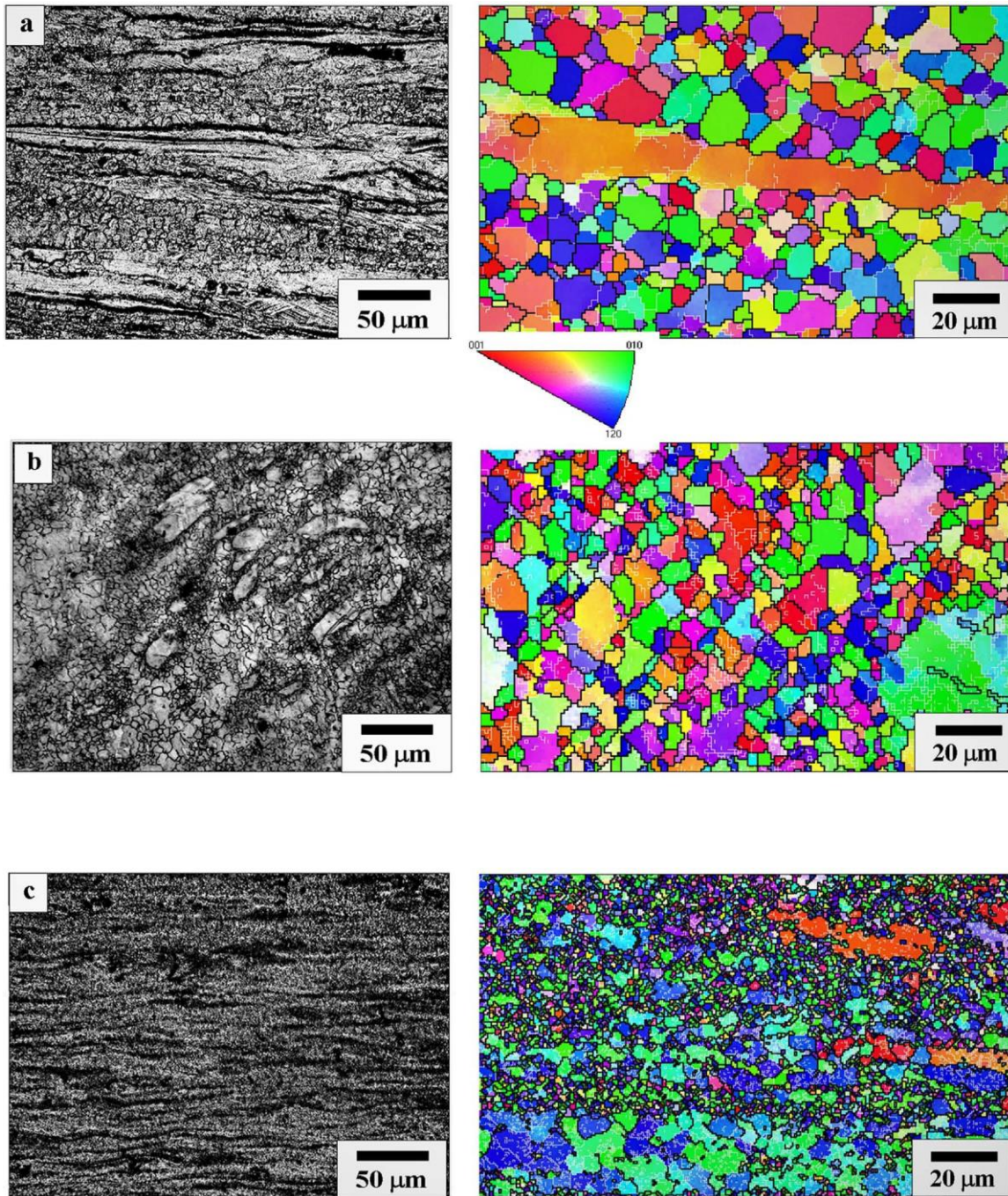
Fig. 2. Typical optical microscopy images (left) and EBSD orientation image maps (right) representing the grain structure in the longitudinal cross-section of the initial hot pressed rod of the alloy MA14 (a) and for the billets after SPD by multiaxial isothermal forging (MIF) (b) and multiaxial forging followed by isothermal rolling (MIF+IR) (c). The grains on the EBSD orientation maps are displayed in inverse pole figure coloring using the same standard stereographic triangle key shown in the inset.

fine-grained structure evolved at high strains during MIF. It can be suggested that finer recrystallized grains were evolved in the regions of localized deformation in a way similar to that in aluminum alloys subjected to equal channel angular pressing [21]).

Further isothermal rolling promoted evolution of the equiaxed fine-grained microstructure into the fine lamellar-like one with alternating bands of recrystallized grains of different sizes, Fig. 2c. The average grain and subgrain size decreased to 2.4 and 1.4 ± 0.2 μm, respectively, testifying continuation of dynamic recrystallization and grain refinement associated with it. The same conclusion can be reasonably drawn from the fact that the coarse grains (more than 20 μm in size) are much less frequently observed in the rolled sheet. Besides, EBSD data have

shown that the grains in the rolled alloy are predominantly surrounded by HABs, Fig. 2c, with the number fraction reaching of 78%, Fig. 3c. Moreover, the fraction of twin boundaries was almost constant during processing. The boundary misorientation angle distributions, Fig. 3, show that primary extension twinning prevails over compression twinning under rolling. As a result, despite severe deformation via the integral processing route involving two deformation techniques, the alloy microstructure remained highly inhomogeneous with a wide grain size distribution, resembling that in the initial hot-pressed rod. Most probably, both data sets - after conventional processing and SPD – bear the same origin associated with the inhomogeneous distribution of primary and secondary phases in the alloy matrix and with the specific
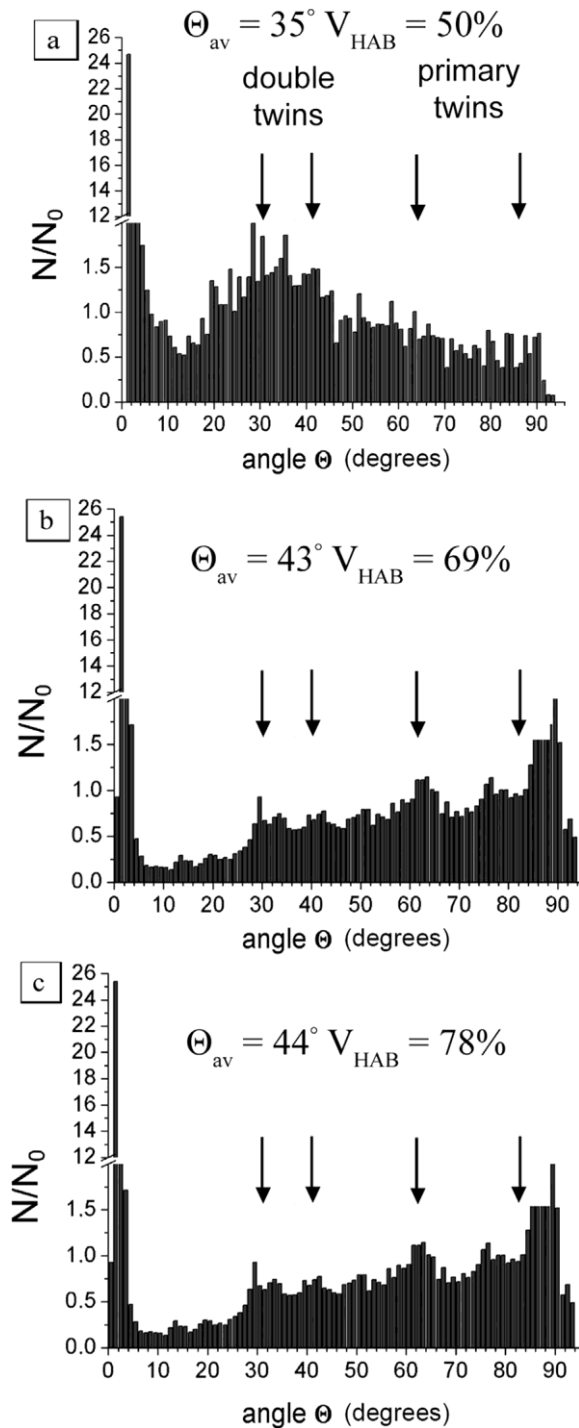
Fig. 3. Grain boundary angular distributions obtained by EBSD for the initial hot pressed rod of the alloy MA14 (a) and for the billets after SPD by multiaxial forging (b) and multiaxial forging followed by isothermal rolling (c). Arrows indicate approximately the intervals of misorientation angles corresponding to different families of twins in the distribution histograms according to [11].

response of the magnesium lattice to micro- and macro-strain localization and twinning.

Thus, the microstructural analysis allows concluding that the alloy grain refinement during forging and rolling under hot-to-warm conditions can occur by both "twinning-based" and "conventional" continuous dynamic recrystallization. In the first case, mechanical twinning operates in preferably oriented coarse grains and twin boundaries are transformed further into random HABs due to formation of

orientation misfit dislocations thought the interaction of the twin boundaries with incoming lattice dislocations (cf. [22]. In the second case, the deformation-induced LABs, which have been presented in the initial rod and those formed under further processing, increased their misorientations and shifted into the high-angle domain of the misorientation spectrum, thus increasing HABs fraction in the course of treatment. As a result, the evolved grains appear to be smaller than the just "twinned" grains [19], creating grain structure inhomogeneity. Besides, one more important process of the elongated structure transformation during hot SPD processing cannot be neglected. This process is known as geometric dynamic recrystallization, which commonly takes place under unidirectional straining at relatively high homologous temperatures [16,26]. During geometric dynamic recrystallization, a substantial grain refinement occurs via grain elongation and thinning. The traces of geometric dynamic recrystallization under rolling can be seen as considerable lengthening of coarse fragments of initial elongated grains, resulting finally in development of equiaxial recrystallized grains via nucleation of boundaries extending across the thickness of initial grains.

3.2. Second phases

The phase compositions of the Mg-Zn-Zr tertiary alloys have been extensively studied [1,23]. Although the main strengthening particles in Mg-Zn-Zr alloys are associated with Mg-Zn intermetallic compounds, e.g. MgZn, $MgZn_2$, and $MgZn_5$, Zr-rich particles, fine precipitates containing Zr appear to form during hot deformation processing, which influences the recrystallization behavior and the microstructure of wrought products. [1,6,21,24,25]. Figs. 4 and 5 show typical TEM and BSE SEM images highlighting secondary phases in the longitudinal cross-section of the processed alloy. It can be seen that the hot-pressed material Fig. 5(a, d, g) contains a high fraction of coarse (up to a few micrometers in size) particles of excess phases (predominantly β-type phases) aligned in strings along the axis of the rod. MIF changed the appearance of these phases significantly. Firstly, the particles refined considerably and the strings became less evident with increasing MIF strain, Fig. 5(b, e, h). Secondly, the particle orientation with respect to the billets axis appeared more random. Thirdly, the distribution of particles in the volume became much more homogeneous. However, further IR resulted in the reappearance of the string-type particle arrangement similar to that in the initial rod, though with notably shorter, narrower and closer spaced strings formed by smaller (on average) particles, Fig. 5(c, f, i).

Typical quantitative parameters – area fraction S, partial area fraction s/S for particles of different sizes and interparticle distance λ – defined in Section 2 and characterizing distributions of both type phases are summarized in Fig. 6 and Table 1. According to these data, the alloy in the initial hot-pressed state has a bimodal size distribution of second phases, Fig. 6a. After MIF, the distribution changed to unimodal, Fig. 6b, and then slightly transformed during rolling, Fig. 6c. These observations can be indicative of two possible processes. The first one, as was mentioned above, is caused by phase refinement through mechanical rupture, which is particularly intense and easy for brittle coarse excess phases. On the other hand, some coarsening of disperse phases could possibly occur during hot MIF deformation. It, then, could continue during hot rolling due to phase coagulation, Fig. 6(f, i) (cf. also Fig. 5c).

It can be also seen from Table 1 that the average phase dimensions as well as their mean area fractions in both longitudinal and transverse cross-sections of the rod and processed billets are almost equal. However, the weak trend to reduce the area fraction can be noticed with accumulated strain in the longitudinal section while the opposite tendency is seen in the transverse section. Most likely, it could be mainly caused by the changes in the particles orientation in the billets volume due to multidirectional straining upon processing. Another reason could be caused by dynamic dissolution of some β-phase plate-shape
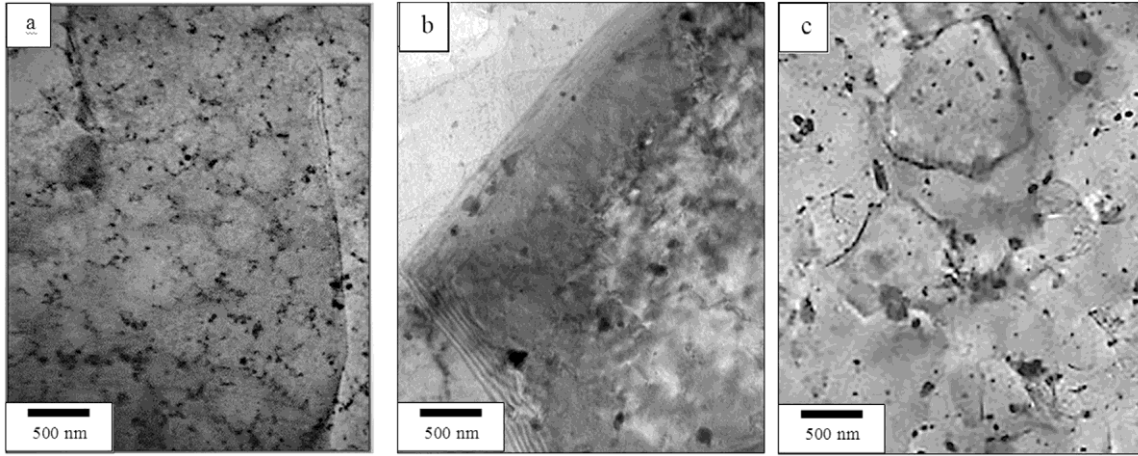
Fig. 4. Bright field TEM structure images of the initial hot pressed rod of the alloy MA14 (a) and of the billets after SPD by multiaxial forging (b) and multiaxial forging followed by isothermal rolling (c).

precipitates and their further re-aging during MIF and IR with actually oriented re-precipitation governed by simultaneous transformations of crystallographic texture discussed below. However, one should bear in mind that according to the equilibrium phase-diagram of the alloy [27] the fraction of these precipitates under processing at 300 °C could not exceed 1%. As a result, for the given alloy microstructure and corresponding phase transformations, the mean values of interphase spacing in the initial rod and processed billets were quite close, suggesting that these phases exert comparable influence on alloy strengthening not only in different directions, but also in all structural states studied, Table 1.

3.3. Crystallographic texture

The evolution of texture during SPD is shown in Fig. 7. In the initial condition, the alloy exhibits the typical for a hot-pressed semi-product fiber texture with the axis of symmetry parallel to the pressing direction and the maximum intensity greater than 12, Fig. 7a. Upon that, the pressing directions in the inverse pole figure (IPF) spread along the line from $< 01\bar{1}0 >$ to $<\bar{2}\,0\,\bar{1}\,0 >$. The microstructure transformations under MIF result in the higher orientation density in a wide range between $<\bar{2}\,\bar{2}\,1>$, $<\,\bar{2}\,\bar{1}\,1>$, $<\,01\,2\,\bar{3}>$ and $< 02\,2\,\bar{1} >$ directions with three relatively weak orientation maxima, Fig. 7b. The maximum intensity of the main and almost unique texture component $\{11\bar{2}2\}$ after MIF was only slightly higher than 5, that is two times weaker than the intensity of the initial fiber texture. As it could be plausibly expected, further rolling resulted in the strong rolling $\{0001\}$ basal texture with the high maximum intensity higher than 21, Fig. 7c.

Thus, three different structural states distinguished by the grain structure, phase composition and texture where produced in the same alloy by different processing routes involving combination of forging and rolling.

3.4. Tensile strength

The mechanical behavior of the alloy in three different microstructural states discussed above is shown in Fig. 8 as nominal stress-strain curves. Corresponding mechanical properties are summarized in Table 2. It is seen that a good balance between the tensile strength and ductility is achieved as a result of SPD processing. The two-step hot-to-warm MIF resulted in appreciable softening in the longitudinal direction of the hot-pressed rod as signaled by a notably reduced yield stress (YS). However, this softening was accompanied by the significant increase in the ductility, measured as the elongation to failure (δ) and by the decrease in the yield stress anisotropy. As a result, the alloy

mechanical response became rather isotropic as reflected by all three parameters measured, including the ultimate tensile strength (UTS), Table 2. The post-MIF rolling gave rise to the alloy strengthening and ductility reduction, as could be reasonably expected. Thus, the YS value was found slightly smaller, while UTS was slightly higher than their respective counterparts in the longitudinal direction of the initial rod. Besides, the YS increased significantly in the transverse direction, while the UTS change was less pronounced and its value remained smaller than that in the initial condition. As it can be compared with the alloy MIF state, rolling resulted in reduction in ductility in both directions. However, the elongation to failure after IR was still by far larger than that in the initial semi-product.

4. Discussion

The mechanical behavior of the alloy is controlled by its microstructure and texture. It has long been established that strengthening mechanisms in alloys are associated with factors increasing the resistance to dislocation motion. The main mechanisms include, but are not limited to, mechanical blocking of dislocation slip by grain (sub-grain) boundaries and/or foreign particles, pinning of dislocations by solute atoms and increasing total dislocation density by strain hardening. Conventionally, the alloy strengthening can be estimated as a cumulative effect of additive contributions exerting influence on dislocation initiation and motion [14,28] :

$$YS = YS_{Mg} + \Delta YS_{SS} + \Delta YS_{GBS} + \Delta YS_{PS} + \Delta YS_{TS} \qquad (1)$$

where YS stands for the yield stress which is composed the following constituents: YS_{Mg} is the yield stress of a pure coarse-grained magnesium associated with dislocation storage, ΔYS_{SS} stands for solid solution strengthening, ΔYS_{GBS} refers to grain boundary strengthening, ΔYS_{PS} is particle strengthening and ΔYS_{TS} is strengthening due to the texture effect. The effect of mechanical twinning is not specified here as an independent strengthening mechanism since the twin boundaries act as the barriers for dislocation motion in the same way to other high-angle grain boundaries.

All these strengthening factors were evaluated and summarized in Table 3. The first and the second term were taken from the available reference data [29,30], the grain boundary strengthening was estimated using the present experimental data and the Hall-Petch relation.

The Orowan's equation for point obstacles [14] gives the strength contribution due to bowing of precipitates as

$\sigma_{Or} = MmGb\Phi \ln((\lambda/d)/2\bar{b})/2\pi\,(\lambda/d)$, where $M = 6.5$ is the Taylor orientation factor [1], $m=0.85$ is the statistical coefficient
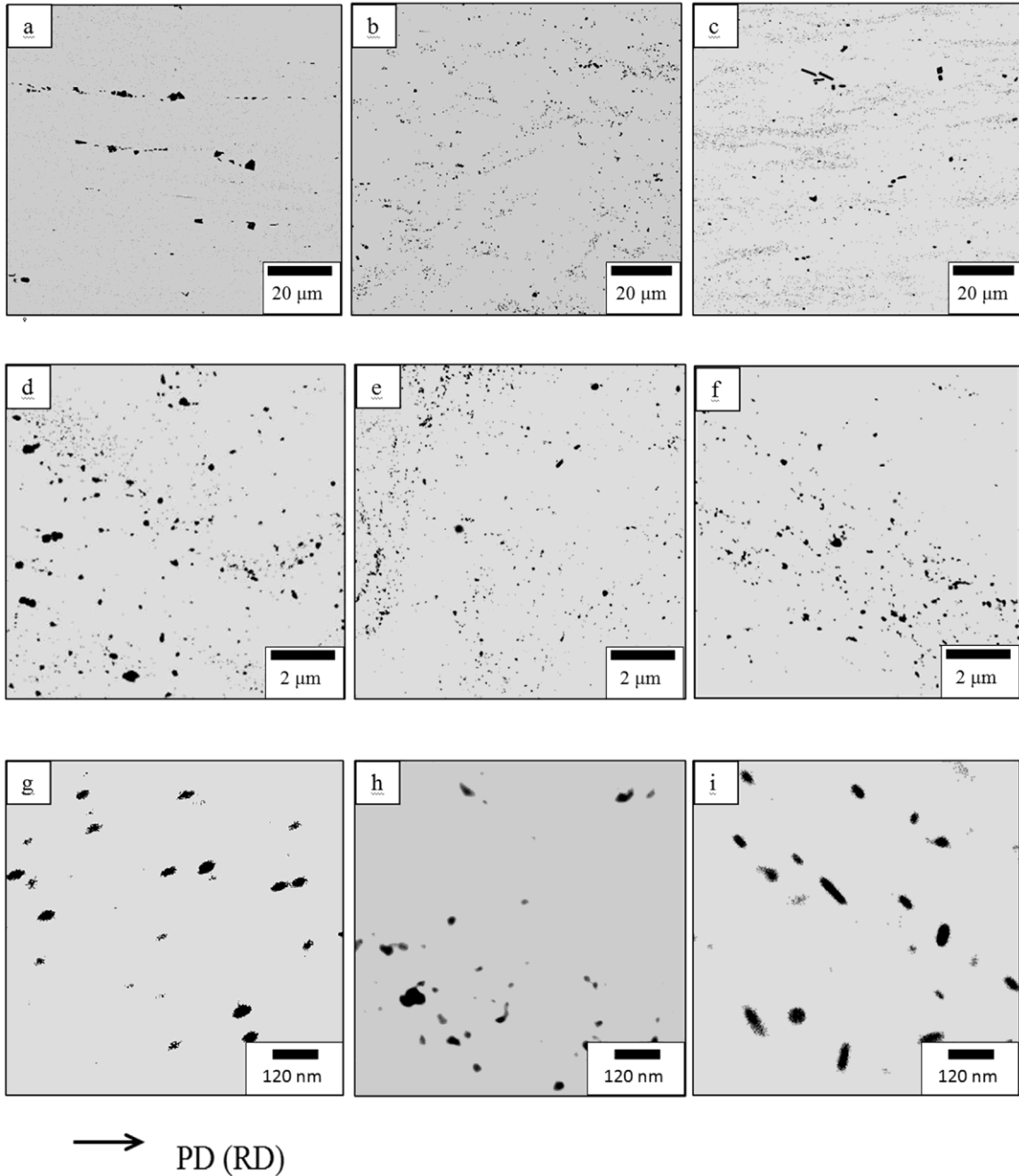
Fig. 5. BSE images showing the typical distributions of secondary phases at different magnifications in the longitudinal cross-sections of the initial hot pressed rod of the alloy MA14 (a) and of the billets after SPD by multiaxial forging (b) and multiaxial forging followed by isothermal rolling (c).

relating the microscopic flow stress of a single crystal with a random distribution of particles with the flow stress determined from the average inter-particle distance [14]. $G = 20.2\,\text{GPa}$ is the shear modulus [1], $b = 3.2 \times 10^{-10}$ m is the magnitude of the Burgers vector of a-dislocation in magnesium [1,31] and $\Phi = \frac{1}{2}(1+1/(1-v)) = 0.25$ is the average coefficient characterizing the edge and twin dislocations-particles interaction ($v = 0.33$ is the Poisson ratio). The contribution of texture was found as the difference between the experimentally measured conventional yield stress and the sum of all other strengthening factors involved.

Based on these considerations, it is plausible to conclude that two factors ensure the major strengthening effect under SPD – grain structure and texture transformations. Among these two, grain refinement is associated with the significant increase in the volume fraction of grain boundaries during MIF and IR, giving rise thereby to considerable Hall-Petch and substructure hardening. Increasing the amount of grains with favorable orientation for basal slip is associated with weak pyramidal texture created during MIF. This promoted the increase in the alloy ductility. IR after MIF gave rise to further grain refinement and formation of ultrafine-grain structure with a fairly strong texture.

One can conclude, therefore, that processing of the MA14 alloy via a combination of hot-to-warm forging and further rolling has promoted significant grain refinement and provided the main contribution to the alloy strength. The beneficial synergistic effect is obtained with a superior balance of deformation characteristics, which outperform those commonly reported for conventional products. The hot-pressed rod showed the pronounced asymmetry in the yield stress while the tensile strength was almost isotropic, Table 2. It is clear that the hardening rate
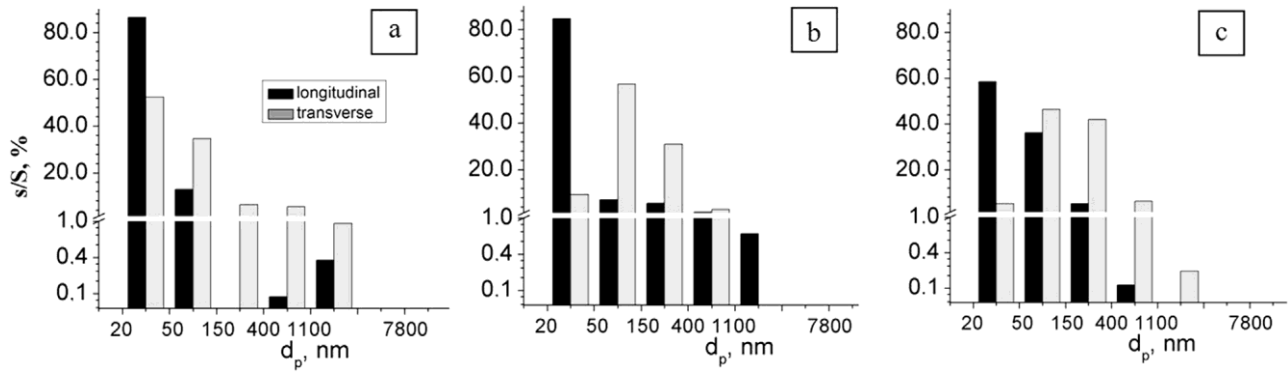
Fig. 6. Partial area fractions of secondary phases with different mean sizes (equivalent particle diameter), d_p, in the longitudinal and transverse sections of the initial hot pressed rod of the alloy MA14 (a) and of the billets after SPD by multiaxial forging (b) and multiaxial forging followed by isothermal rolling (c).

Table 1
Characteristics of second phases in the longitudinal/transverse sections of the alloy MA14 (SEM-BSE analysis).

Condition	$\bar{d}$, nm	S, %	λ, nm
Hot-pressed rod	63/60	4.4/3.4	200/210
+ MIF	68/63	3.4/3.3	230/270
+ MIF + IR	68/65	3.3/3.9	270/240

in the transverse direction, Fig. 8a, is higher than that in the longitudinal one, Fig. 8b. The observed difference in the hardening rate might appear as a result of different activity of the basal slip system and/or the effect of the anisotropic distribution of second phases. The fiber texture facilitates a greater basal slip activity in the transverse direction thus lowering the corresponding yield stress value with the concomitantly increasing rate of dislocation accumulation and longer strain hardening stage, Table 2. Reduction of the longitudinal yield stress and its anisotropy after MIF is associated primarily with the texture effect. Formation of pyramidal texture in the billet during MIF led to a lesser strength owing to the increased basal slip activity upon
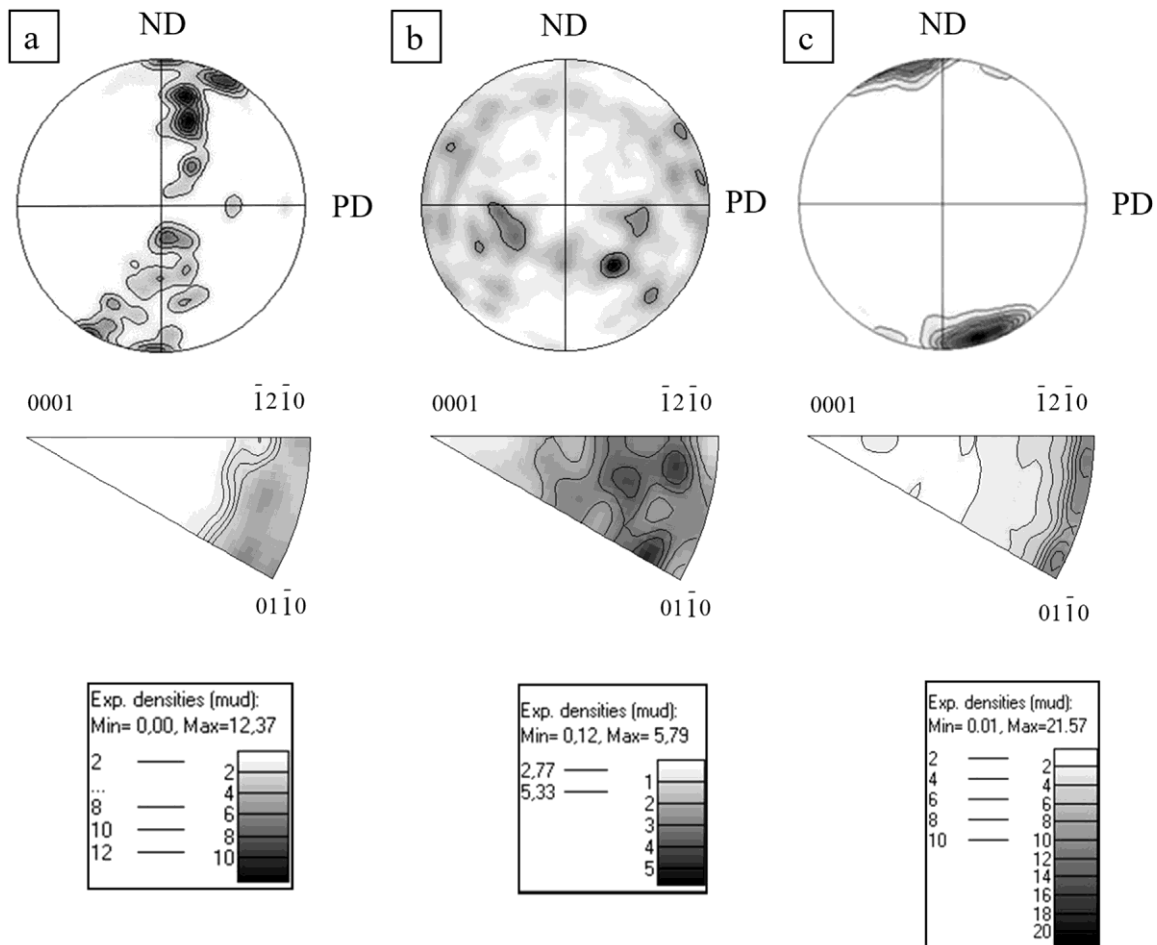
Fig. 7. Fig. 5. Direct {0001} and inverse pole figures and corresponding texture intensities in the initial hot pressed alloy rod (a) and that after MIF (b) and MIF+IR processed billets (c). In (a) and (b) the inverse pole figures were plotted for PD, in (c) - for RD.
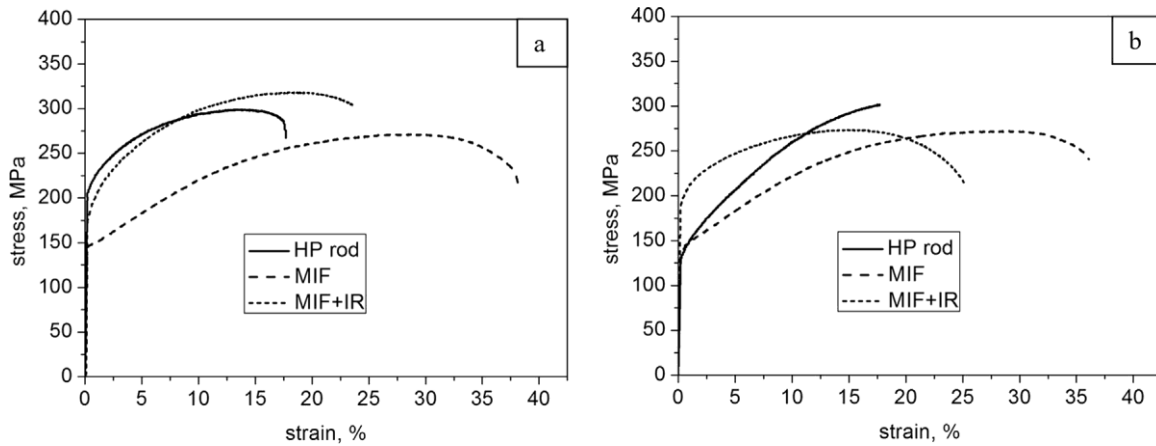
Fig. 8. The alloy room-temperature true stress-strain tensile curves for the specimens aligned with longitudinal (LT) (a) and transverse (TL) (b) directions of the working billet.

Table 2
The alloy tensile strength parameters at room temperature.

Condition	YS, MPa		UTS, MPa		δ, %	
	LT	TL	LT	TL	LT	TL
Initial rod	200*	130	310	300	17	19
After MIF	145	135	280	275	37	34
After MIF and IR	180	195	320	275	24	25

(*- the confidence interval for YS and UTS equals ± 5 MPa and for δ it is ± 2%)

Table 3
The alloy strengthening factors in longitudinal/transverse directions.

Condition	YS_{Mg}, MPa	ΔYS_{SS}, MPa	ΔYS_{PS}, MPa	ΔYS_{GBS}, MPa	ΔYS_{TS}, MPa
HP rod	20/20	20/20	27/29	58/42	75/19
MIF		20/20	40/36	59/59	6/0
MIF + IR		20/20	36/43	93/93	11/19

tensile testing of the LT samples. As opposes to this trend, the following rolling is accompanied by the formation of {0001} basal texture that impeded dislocation motion on the basal systems and increased the alloy strength, providing the yield strength almost equal to that in the hot-pressed rod in longitudinal direction and even higher in the TL samples. The same reasons caused the ductility reduction in the rolled specimens. However, their elongations were still considerably higher than that in the initial hot-pressed rod, where the basal planes were practically unavailable for dislocation glide. Such a behavior was associated with grain refinement since a larger number of grains were oriented favorably for basal dislocation slip.

It could be expected that SPD compromised the contribution from particle strengthening to some extent owing to refinement of coarse excess phases, Fig. 5. Besides, some (re)precipitation obviously took place in all stages of deformation processing, c.f. Figs. 4 and 5. However, due to relatively large values of the mean planar interparticle spacing measured, Table 1, any strengthening/softening effects caused by Mg-Zn phase changes during SPD could be insignificant and be only within 10-15 MPa in accordance to the Orowan hardening equation. On the other hand, the elimination of the stringer-type particles of excess phases, decreasing their size and increasing homogeneity of their distribution during SPD, Fig. 6, could provide more homogeneous deformation and thus additionally enhance the alloy ductility.

Thus, because precipitation of the main strengthening Mg-Zn phases was not significant under isothermal processing conditions used, no substantial changes in the effect of precipitation hardening after MIF and further rolling were noticed. The texture and grain refinement resulting from SPD exert a stronger influence on the mechanical

properties of the fine-grained alloy processed by MIF and rolling in general and ductility in particular. Moreover, the texture changes were considered to be the main reason for alleviating the strong yield stress anisotropy in the initial rod.

Finally, we should note that clarifying the role of precipitates in the recrystallization process on every deformation stage remains to be an open issue of paramount importance. Addressing this fundamental problem requires a dedicated investigation, which is beyond the scope of the present work.

5. Conclusions

1. The thermo-mechanical processing of the Mg-Zn-Zr alloy MA14 (ZK60) combining isothermal multi-step forging and rolling has been proven effective for fabrication of magnesium sheets with a fairly homogeneous completely recrystallized microstructure having very fine grain size of 1–2 µm.
2. Hot-to-warm deformation processing of fine grained sheets and strong basal texture provided a good balance between strength and ductility at ambient temperature. Both strength and ductility were found remarkably improved in comparison to those of the commercial hot-pressed rod.
3. Grain refinement and texture evolution during SPD processing were found to be the key factors affecting the mechanical response of the fine grained material. The increasing volume fraction of grains oriented favorably for basal slip due to weak pyramidal texture obtained during multi-step forging has promoted the significant gain in ductility. Subsequent isothermal rolling gave rise to further grain refinement and formation of ultrafine-grain structure with strong texture. Although the ductility was compromised to some extent by rolling, the elongation at break of the alloys fabricated in this way was still higher than that in the initial hot-pressed rod due to a larger number of fine grains having a favorable orientation for easy basal dislocation slip.

Acknowledgements

References

[1] B.L. Mordike., P. Lukac, Magnesium Technology, Metallurgy, Design Data, Applications, Springer, New York, 2007.
[2] J. Hirsch, T. Al-Samman, Superior light metals by texture engineering: optimized aluminum and magnesium alloys for automotive applications, Acta Mater. 61 (2013) 818–843.
[3] M. Markushev, A. Vinogradov, Room temperature mechanical properties of sub-microcrystalline commercial aluminum alloys processed by severe plastic

deformation, in: B. Altan (Ed.), Severe Plastic Deformation: Towards Bulk Production of Nanostructured Materials, Nova Science Publishers, New York, 2006, pp. 233–249.

[4] H.W. Höppel, M. Kautz, C. Xu, M. Murashkin, T.G. Langdon, R.Z. Valiev, H. Mughrabi, An overview: fatigue behaviour of ultrafine-grained metals and alloys, Int. J. Fatigue 28 (2006) 1001–1010.

[5] Y. Estrin, A. Vinogradov, Extreme grain refinement by severe plastic deformation: a wealth of challenging science, Acta Materialia 61 (2013) 782–817.

[6] R.R. Mulyukov, R.M. Imayev, et al., Superplasticity of Ultrafine Grained Alloys: Experiment, Theory, Technologies, Nauka, Moscow, 2014.

[7] D. Nugmanov, O. Sitdikov, M. Markushev, Structure of magnesium alloy MA14 after multistep isothermal forging and subsequent isothermal rolling, Phys. Met. Metallogr. 116 (2015) 993–1001.

[8] D.R. Nugmanov, O. Sh. Sitdikov, M.V. Markushev, Grain refinement in the magnesium alloy ZK60 during multi-step isothermal forging, Mater. Sci. Forum 830–831 (2015) 7–10.

[9] ISO Standard 13067:2011, Microbeam analysis - Electron backscatter diffraction - Measurement of average grain size.

[10] ⟨https://caf.ua.edu/wp-content/uploads/docs/JEOL-7000F-Oxford_Channel_5_User_Manual.pdf⟩.

[11] S. Mu, J.J. Jonas, G. Gottstein, Variant selection of primary, secondary and tertiary twins in a deformed Mg alloy, Acta Materialia 60 (2012) 2043–2053.

[12] O. Muransky, M.R. Barnett, D.G. Carr, Investigation of deformation twinning in a fine grained and coarse grained ZM20 Mg alloy: combined in situ neutron diffraction and acoustic emission, Acta Mater. 58 (2010) 1503–1517.

[13] S.I. Wright, M.M. Nowell, J.F. Bingert, A comparison of textures measured using X-ray and electron backscatter diffraction, Met. Mat. Trans. 38 A (2007) 1845–1855.

[14] M.I. Goldshtein, V. S. Litvinov, Metallofizika vysokoprochnykh splavov, Moscow, Metallurgia, 1986.

[15] H. Miura., X. Yang, T. Sakai, Evolution of ultrafine grains in AZ31 and AZ61 Mg alloys during multidirectional forging and their properties, Mater. Trans. 49 (2008) 1015–1020.

[16] F.J. Humphreys, M. Hatherly, Recrystallization and Related Annealing Phenomena, 2nd ed., Elsevier, Oxford, 2004.

[17] I.J. Beyerlein, J. Wang, M.R. Barnett, C.N. Tome, Double twinning mechanisms in magnesium alloys via dissociation of lattice dislocations, Proc. R. Soc. A 468 (2012) 1496–1520.

[18] J. Koike, New deformation mechanisms in fine-grain Mg alloys, Mater. Sci. Forum 419–422 (2003) 189–194.

[19] O. Sitdikov, R. Kaibyshev, Dynamic recrystallization in pure magnesium, Mater. Trans. 42 (2001) 1928–1937.

[20] (a) R.O. Kaibyshev, O.S. Sitdikov, Phys. Met. Metallogr. 73 (1992) 635–642;
(b) A. Galiyev, R. Kaibyshev, G. Gottstein, Acta Mater. 49 (2001) 1199–1207;
(c) O. Sitdikov, R. Kaibyshev, T. Sakai, Mater. Sci. Forum 419–422 (2003) pp. 521–26.

[21] Sitdikov, O., Avtokratova, E., Sakai, T., Tsuzaki, K. Metallurgical and Materials Transactions A 44(2):1087–1100.

[22] (a) R.O. Kaibyshev, O.S. Sitdikov, Phys. Met. Metallogr. 73 (1992) 635–642;
(b) A. Galiyev, R. Kaibyshev, G. Gottstein, Acta Mater. 49 (2001) 1199–1207;
(c) O. Sitdikov, R. Kaibyshev, T. Sakai, Mater. Sci. Forum (2003) 419–422 pp. 521–26.

[23] S. Bhan, A. Lal, The Mg-Zn-Zr system (magnesium-zinc-zirconium), J. Phase Equilib. 14 (5) (1993) 634–637.

[24] L. Lin, Z. Liu, L. Chen, F. Li, Tensile properties and strengthening mechanisms of Mg—Zn—Zr alloys, Met. Mater. Int. 10 (6) (2004) 507–512.

[25] T. Bhattacharjee, C.L. Mendis, T.T. Sasaki, T. Ohkubo, K. Hono, Effect of Zr addition on the precipitation in Mg–Zn-based alloy, Scrip. Mater. 67 (12) (2012) 967–970.

[26] M.E. Kassner, S.R. Barrabes, New developments in geometric dynamic recrystallization, Mater. Sci. Eng. A 410-411 (2005) 152–155.

[27] J.D. Robson, C. Paa-Rai, The interaction of grain refinement and ageing in magnesium–zinc–zirconium (ZK) alloys, Acta Mater. 95 (2015) 10–19.

[28] P. Fu, L. Peng, H. Jiang, W. Ding, C. Zhai, Tensile properties of high strength cast Mg alloys at room temperature: a review, China Foundry 11 (4) (2014) 277–286.

[29] K. Edalati, A. Yamamoto, et al., High-pressure torsion of pure magnesium: evolution of mechanical properties, microstructures and hydrogen storage capacity with equivalent strain, Scrip. Mater. 64 (2011) 880–883.

[30] H. Somekawa, Y. Osawa, T. Mukai, Effect of solid-solution strengthening on fracture toughness in extruded Mg–Zn alloys, Scrip. Mater. 55 (2006) 593–596.

[31] N. Wang, C.I. Chang, C.J. Lee, H.K. Lina, J.C. Huang, Texture and weak grain size dependence in friction stir processed Mg–Al–Zn alloy, Scrip. Mater. 55 (2006) 637–640.